# Cage-Forming Compounds in the Ba−Rh−Ge System: From Thermoelectrics to Superconductivity

M. Falmbigl,[†] F. Kneidinger,[‡] M. Chen,[†,§] A. Grytsiv,[†] H. Michor,[‡] E. Royanian,[‡] E. Bauer,[‡]
H. Effenberger,[⊥] R. Podloucky,[†,§] and P. Rogl*,[†]

[†]Institute of Physical Chemistry, University of Vienna, Währingerstrasse 42, A-1090 Wien, Austria
[‡]Institute of Solid State Physics, Vienna University of Technology, Wiedner Hauptstrasse 8−10, A-1040 Wien, Austria
[§]Center for Computational Materials Science, University of Vienna, Sensengasse 8/7, A-1090 Wien, Austria
[⊥]Institute of Mineralogy and Crystallography, University of Vienna, Althanstrasse 14, A-1090 Wien, Austria

S *Supporting Information*

ABSTRACT: Phase relations and solidification behavior in the Ge-rich part of the phase diagram have been determined in two isothermal sections at 700 and 750 °C and in a liquidus projection. A reaction scheme has been derived in the form of a Schulz−Scheil diagram. Phase equilibria are characterized by three ternary compounds: τ_1-BaRhGe$_3$ (BaNiSn$_3$-type) and two novel phases, τ_2-Ba$_3$Rh$_4$Ge$_{16}$ and τ_3-Ba$_5$Rh$_{15}$Ge$_{36-x}$, both forming in peritectic reactions. The crystal structures of τ_2 and τ_3 have been elucidated from single-crystal X-ray intensity data and were found to crystallize in unique structure types: Ba$_3$Rh$_4$Ge$_{16}$ is tetragonal ($I4/mmm$, $a = 0.65643(2)$ nm, $c = 2.20367(8)$ nm, and $R_F = 0.0273$), whereas atoms in Ba$_5$Rh$_{15}$Ge$_{36-x}$ ($x = 0.25$) arrange in a large orthorhombic unit cell ($Fddd$, $a = 0.84570(2)$ nm, $b = 1.4725(2)$ nm, $c = 6.644(3)$ nm, and $R_F = 0.034$). The body-centered-cubic superstructure of binary Ba$_8$Ge$_{43}$□$_3$ was observed to extend at 800 °C to Ba$_8$Rh$_{0.6}$Ge$_{43}$□$_{2.4}$, while the clathrate type I phase, κ_I-Ba$_8$Rh$_x$Ge$_{46-x-y}$□$_y$, reveals a maximum solubility of $x = 1.2$ Rh atoms in the structure at a vacancy level of $y = 2.0$. The cubic lattice parameter increases with increasing Rh content. Clathrate I decomposes eutectoidally at 740 °C: $\kappa_I \Leftrightarrow$ (Ge) + κ_{IX} + τ_2. A very small solubility range is observed at 750 °C for the clathrate IX, κ_{IX}-Ba$_6$Rh$_x$Ge$_{25-x}$ ($x \sim 0.16$). Density functional theory calculations have been performed to derive the enthalpies of formation and densities of states for various compositions Ba$_8$Rh$_x$Ge$_{46-x}$ ($x = 0-6$). The physical properties have been investigated for the phases κ_I, τ_1, τ_2, and τ_3, documenting a change from thermoelectric (κ_I) to superconducting behavior (τ_2). The electrical resistivity of κ_I-Ba$_8$Rh$_{1.2}$Ge$_{42.8}$□$_{2.0}$ increases almost linearly with the temperature from room temperature to 730 K, and the Seebeck coefficient is negative throughout the same temperature range. τ_1-BaRhGe$_3$ has a typical metallic electrical resistivity. A superconducting transition at $T_C = 6.5$ K was observed for τ_2-Ba$_3$Rh$_4$Ge$_{16}$, whereas τ_3-Ba$_5$Rh$_{15}$Ge$_{35.75}$ showed metallic-like behavior down to 4 K.

τ_1, Ba$_5$Rh$_{15}$Ge$_{35.75}$ τ_2, Ba$_3$Rh$_4$Ge$_{16}$

κ_I, Ba$_8$Rh$_x$Ge$_{46-x-y}$□$_y$
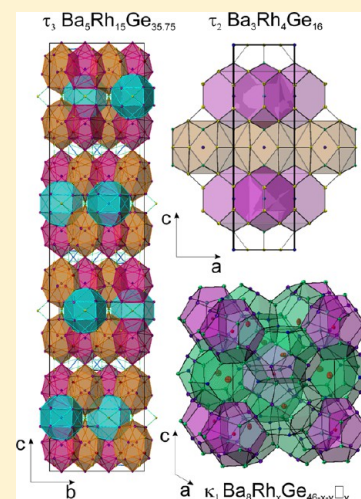
1. INTRODUCTION

With the development of the phonon glass−electron crystal concept,[1,2] intermetallic clathrates were considered as promising materials for thermoelectric applications.[3] Particularly clathrate type I materials have been studied intensively, and the results have been summarized recently.[4,5] Up to now, some of the most promising candidates were Ba−Ge-based solid solutions, for which it was demonstrated that transition metals such as Mn, Fe, Co,[6] Ni, Cu,[7] Zn,[8] Pd, Ag,[7] Cd,[8] Pt, and Au[7] can significantly stabilize a clathrate I phase deriving from the binary compound Ba$_8$Ge$_{43}$□$_3$, which exists only in a very limited temperature range from 770 to 810 °C.[9] Hitherto, the existence of a clathrate I Ba$_8$Rh$_x$Ge$_{46-x-y}$□$_y$ was not reported. Thus, the aim of this investigation is (i) to explore the formation and homogeneity range of the corresponding clathrate I phase, (ii) to establish the phase relations in the Ge-rich part of the Ba−Rh−Ge system, (iii) to characterize the crystal structure of new ternary phases, and (iv) to provide information on the physical properties of the compounds involved. The results of density functional theory (DFT) calculations are included in order to analyze the trend of thermodynamic stability and the change of the density of states (DOS) as a function of Rh doping in the clathrate I phase Ba$_8$Rh$_x$Ge$_{46-x}$.

2. EXPERIMENTAL DETAILS

2.1. Sample Preparation and Characterization. Samples for phase analyses and crystal structures were prepared by argon arc melting from elemental ingots (Ba, 99.9 mass %; Rh, 99.99 mass %; Ge, 99.999 mass %) on a water-cooled copper hearth. To compensate for losses of Ba, ~2 wt % was added beforehand. For all samples, the weight loss was below 2 wt %. The arc-melted buttons were cut into two pieces and sealed in evacuated quartz tubes. All samples were annealed for 7 days at 750 and 700 °C and afterward characterized by powder X-ray diffraction (PXRD), differential thermal analysis (DTA), and electron probe microanalysis (EPMA). For PXRD, a Huber imaging-plate system

Table 1. Crystallographic Data on the Solid Phases of the Binary Systems Ba−Ge (>70 atom % Ge) and Rh−Ge (>50 atom % Ge) and the Ternary System Ba−Rh−Ge

phase	space group	structure type	lattice parameter [nm]			ref
			a	b	c	
Ge, <938 °C	$Fd\bar{3}m$	C_{diam}	0.5659(7)			37
Ba_8Ge_{43}, 770− 810 °C	$Ia\bar{3}d$	Ba_8Ge_{43}	2.13123(5)			9
$BaGe_5$, 450−608 °C	$Pmna$	$BaGe_5$	1.0727(1)	0.92844(7)	1.4794(1)	23
$Rh_{17}Ge_{22}$, <1000 °C	$I\bar{4}2d$	$Rh_{17}Ge_{22}$	0.5604(2)		7.845(2)	38
κ_{IX}-$Ba_6Rh_xGe_{25-x}$	$P4_132$	Ba_6Ge_{25}	1.45361(3)			$x = 0.16^a$
			1.45495(1)			$x = 0.0^a$
κ_I-$Ba_8Rh_xGe_{46-x-y}\square_y$	$Pm\bar{3}n$	K_4Ge_{23-x}	1.06932(2)			$x = 1.2, y = 2^a$
τ_1-$BaRh_{1-x}Ge_{3+x}$	$I4mm$	$BaNiSn_3$	0.458085(4)		1.02403(1)	$x = 0.23^a$
			0.45550(1)		1.02802(2)	$x = 0.14^a$
			0.45240(3)		1.0274(1)	$x = 0^{22}$
τ_2-$Ba_3Rh_4Ge_{16}$, <785 °C	$I4/mmm$	$Ba_3Rh_4Ge_{16}$	0.65643(2)		2.20367(8)	a
τ_3-$Ba_5Rh_{15}Ge_{35.75}$, <830 °C	$Fddd$	$Ba_5Rh_{15}Ge_{36-x}$	0.84750(2)	1.4725(2)	6.644(3)	$x = 0.25^a$

^{a}This work.

equipped with a monochromator (Cu $K\alpha_1$ radiation) was used. A detailed evaluation of the powder patterns was performed via Rietveld refinements employing the *FullProf* program.[10] Scanning electron microscopy images and EPMA measurements using an energy-dispersive X-ray (EDX) detector (Oxford Instruments) were carried out on a Zeiss Supra 55VP instrument. Single-crystal X-ray diffraction data at 300 K (for the clathrate I phase also at 200 and 100 K) were collected on a four-circle Nonius Kappa diffractometer equipped with a CCD area detector and monochromated Mo $K\alpha$ radiation, whereby isothermal temperatures for the crystal, mounted with transparent varnish on a glass rod, were assured by a continuous stream of nitrogen gas enclosing the crystal at a preset temperature. Single-crystal X-ray data were analyzed using the *SHELX* program system.[11] DTA measurements were performed on Netzsch DSC 404C equipment under an argon atmosphere with an uncertainty in the temperature of ±5 °C.

The single-phase samples for physical property measurements (∼2 g each) were synthesized in the same way as those described above (BaRhGe₃, as cast) and annealed at 800 °C (clathrate I) and 770 °C ($Ba_3Rh_4Ge_{16}$ and $Ba_5Rh_{15}Ge_{35.75}$), respectively. Resistivity measurements at various magnetic fields were performed in a Cryogenic ³He bath top-loading cryostat with a maximum field of about 12.5 T. The accessible temperature covers the range from 300 mK to room temperature. The samples were mounted on a platform, with the current flowing parallel to the applied magnetic field using a four-probe technique. The resistivity was measured using a high-precision Lakeshore bridge with a 13.7 Hz alternating-current technique and 10 mA excitation current. Specific heat measurements were performed on a PPMS Quantum Design 6000 with the relaxation calorimetry technique from 2 to 20 K in magnetic fields of 0−2 T. An additional zero-field specific heat measurement was performed in the temperature range from 3 to 80 K employing an adiabatic step-heating technique (∼1 g sample mass). At temperatures above 300 K, the electrical resistivity and Seebeck coefficient were measured simultaneously with an ULVAC ZEM3 system.

2.2. DFT Calculations. DFT calculations were carried out by the Vienna ab initio Simulation Package.[12] The exchange-correlation functional was parametrized in terms of the local density approximation according to Ceperley and Alder.[13] The electron−ion interaction is treated within the framework of the projector augmented wave method.[14,15] The valence state configuration for construction of the pseudopotentials included the 5s, 5p, and 6s states for Ba, the 5s and 4d states for Rh, and the 3d, 4s, and 4p states for Ge. For structural relaxations, i.e., total energy minimization and relaxation of atomic forces, a 5 × 5 × 5 k-point grid according to Monkhorst and Pack[16] resulted in well-converged structural parameters. For calculations of the electronic DOSs, a dense 11 × 11 × 11 k-point mesh was constructed.

3. BINARY BOUNDARY SYSTEMS

For the Ge-rich part (>70 atom % Ge) of the Ba−Ge system, the phase diagram reported by Okamoto[17] was accepted, which was adapted from refs 18 and 19. The Rh−Ge boundary system (≥50 atom % Ge) was taken from Massalski.[20] The crystallographic data of all relevant phases are listed in Table 1. No contradictions to the accepted binary boundary systems were observed throughout all of the investigations carried out within this work.

4. RESULTS AND DISCUSSION

4.1. Clathrate I Solid Solution at 800 °C. The formation and solubility limits of the clathrate I phase $Ba_8Rh_xGe_{46-x-y}\square_y$ at 800 °C were studied by PXRD and EPMA on samples with nominal compositions $x = 1-4$ and $y = 0$. In all cases, a successful indexation of the clathrate I phase with the crystal structure of K_4Ge_{23-x} was possible. The sample with $x = 1$ revealed Ge as the only secondary phase; all other samples ($x \geq 2$) revealed the presence of Ge and an increasing amount of τ_2 with increasing Rh content. Careful analysis of the lattice parameters and the EPMA data revealed a solubility range of Rh in $Ba_8Ge_{43}\square_3$ extending into the ternary region up to the composition $Ba_8Rh_{1.2}Ge_{42.8}\square_{2.0}$ (see Figure 1). In comparison to the isovalent Co, for which a maximum solubility of 2.5 atoms/unit cell was reported,[6] the solubility of the larger Rh atoms (r_{Rh} = 0.1345 nm and r_{Co} = 0.1252 nm[21]) decreases significantly but leads to a typical enlargement of the cubic lattice. The Ba content of the sample $Ba_8Rh_1Ge_{45}$ is, according to EPMA data, slightly higher than that for the other samples, indicating a higher concentration of vacancies ($\square$). Consistent with this observation, Rietveld refinements of the PXRD patterns—fixing the Rh content to the EPMA data—result in a composition of $Ba_8Rh_{0.6}Ge_{43}\square_{2.4}$ for the sample with the smallest Rh content and $Ba_8Rh_{1.2}Ge_{42.8}\square_{2.0}$ for all others exceeding the solubility limit. EPMA data of the as-cast alloy $Ba_8Rh_1Ge_{45}$ result in a Rh content of 1.7 atom %, whereas during annealing at 800 °C, the Rh content shrinks to 1.2 atom % and superstructure reflections of $Ba_8Ge_{43}\square_3$[9] appear clearly observable in the powder pattern. With respect to clathrate type I ($Pm\bar{3}n$, a_0), $Ba_8Ge_{43}\square_3$ crystallizes in an 8 times larger unit cell ($a = 2a_0$) with space group $Ia\bar{3}d$ because of a full order among Ge atoms and vacancies. For details, see ref 9. Rietveld refinements of the superstructure cell revealed a Rh content of 0.7 atoms/ formula unit in the 24c position, which remains completely vacant
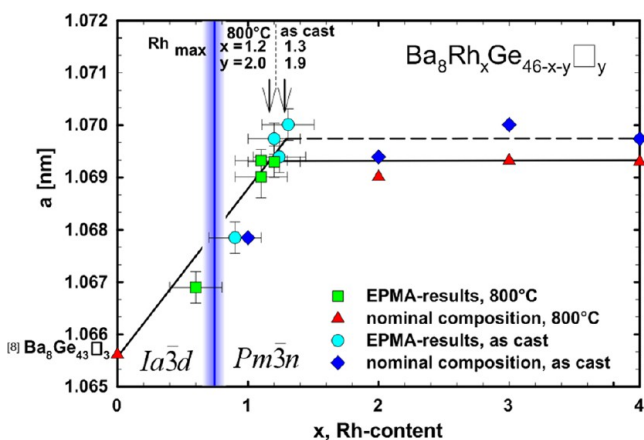
Figure 1. Compositional dependence of the lattice parameters for $Ba_8Rh_xGe_{46-x-y}\square_y$ quenched from 800 °C, compared to as-cast data. The lattice parameters of $Ba_8Ge_{43}\square_3$ and for the compound with $x = 0.6$ were taken as $a/2$ of the superstructure of clathrate I.[9] The blue vertical bar indicates the symmetry change from the superstructure to the clathrate I structure.

Figure 2. Micrographs (backscatter detector) of selected samples at 700 °C. The corresponding data are given in Table S1 (Supporting Information); sample positions are indicated by black circles in Figure 3.

Figure 3. Partial isothermal section at 700 °C. Sample numbers correspond to the numbers given in Table S1 (Supporting Information) and Figure 2.

in the fully ordered structure of binary $Ba_8Ge_{43}\square_3$. This result is in sound agreement with the 0.6 Rh atoms/formula unit found by EPMA. The as-cast sample with EPMA composition $Ba_8Rh_{0.9}Ge_{43.1}\square_2$ does not show superstructure reflections, indicating the breakdown of the vacancy ordering and a random mixture of all three species (Rh, Ge, and $\square$) and thus a reduction of the crystal symmetry to the conventional clathrate I structure with the smaller unit cell (a_0). This observation may indicate that the substitution of Ge atoms by Rh atoms, instead of exclusively filling vacant positions, starts between a Rh content of 0.6 and 0.9 atoms/formula unit (highlighted by the blue vertical line in Figure 1). The phase transition might be of second order because the symmetries of the structure and superstructure exhibit a crystallographic group−subgroup relation. Interestingly, all samples reveal a slightly higher Rh content in the clathrate phase in as-cast conditions (see Figure 1), indicating that the temperature of 800 °C is not the temperature at which the maximum solubility of Rh is reached in the clathrate I phase.

4.2. Phase Equilibria in the Ternary System Ba−Rh−Ge (>60 atom % Ge). *4.2.1. Phase Equilibria at 700 °C.* The phase relations at 700 °C based on PXRD as well as EPMA data are summarized in Table S1 (Supporting Information). Corresponding micrographs representing the three-phase equilibria are shown in Figure 2. The isothermal section is drawn in Figure 3. Only one ternary phase, τ_1-BaRhGe$_3$ crystallizing in the BaNiSn$_3$ structure type,[22] exhibits a solubility range (defined by EPMA measurements). Because the Ba content in τ_1-BaRhGe$_3$ for all measurements does not deviate significantly from 20 atom %, partial substitution of Rh by Ge in the 2a site rather than vacancy formation is suggested ($BaRh_{1-x}Ge_{3+x}$), although in this case, the Rietveld refinement of the multiphase samples does not allow any conclusion on substitution or vacancy formation. The maximum solubility of Ge was detected in an alloy located in the three-phase region with τ_2 and κ_{IX} being $x = 0.22$. The lattice parameter a is slightly increasing with increasing Ge content, whereas c is slightly decreasing. Compared to the lattice parameters of the as-cast τ_1-BaRhGe$_3$ (stoichiometric composition), the unit cell volume is increased by 2%. The existence of the fully ordered structure, reported earlier,[22] was not investigated here. For the binary phases $Rh_{17}Ge_{22}$ and κ_{IX}, the solubility of the third
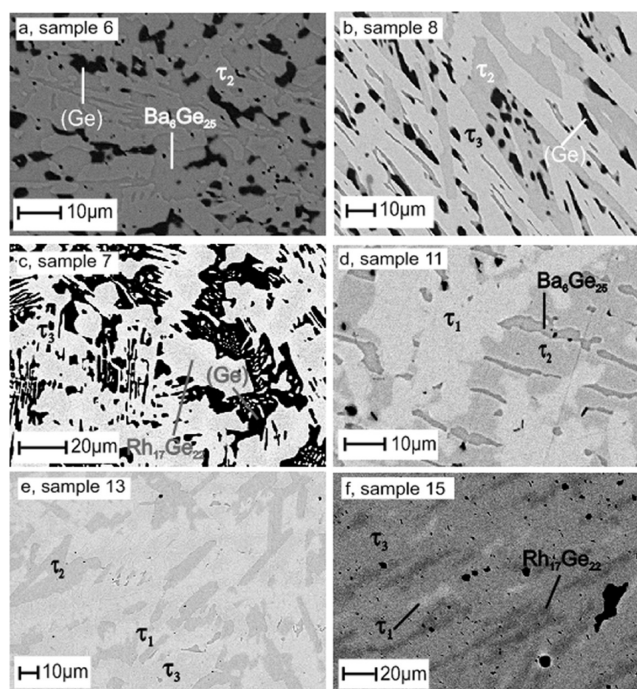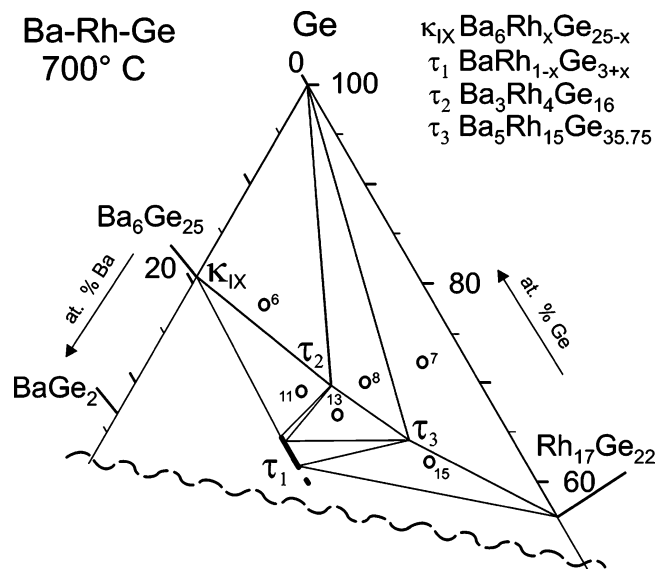
element was below the detection limits. The three-phase equilibrium (Ge) + κ_{IX} + τ_2, as observed in sample 6 (see Figure 2), clearly documents the fact that a type I clathrate phase does not form at 700 °C. The low-temperature phase, BaGe$_5$, reported by Aydemir et al.,[23] was not observed in this investigation.

4.2.2. Phase Equilibria at 750 °C and Invariant Reactions up to 830 °C. In contrast to the isothermal section at 700 °C, the clathrate I phase $Ba_8Rh_xGe_{46-x-y}\square_y$ exists at 750 °C as a truly ternary phase and extends to a maximum Rh content of $x_{max} = 1.2$ in equilibrium with τ_2 and κ_{IX} (see Figure 4). The solubility limit is practically the same as that at 800 °C. Because

Figure 4. Partial isothermal section at 750 °C. Sample numbers correspond to the numbers given in Table S2 (Supporting Information) and Figure 5.
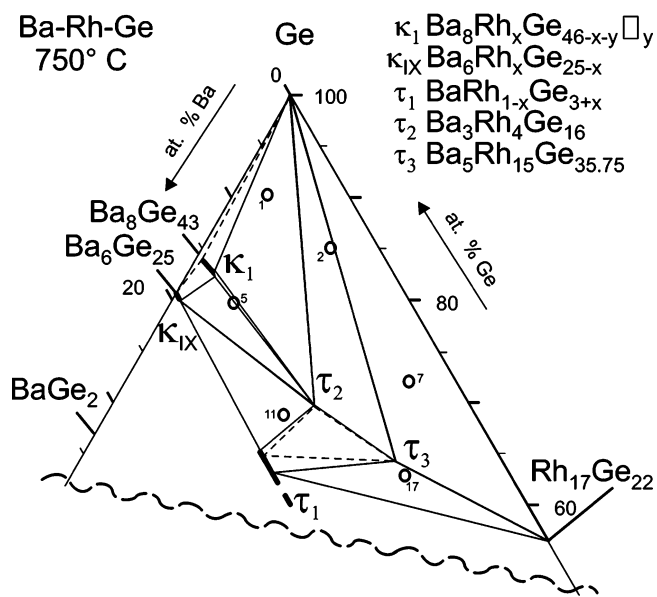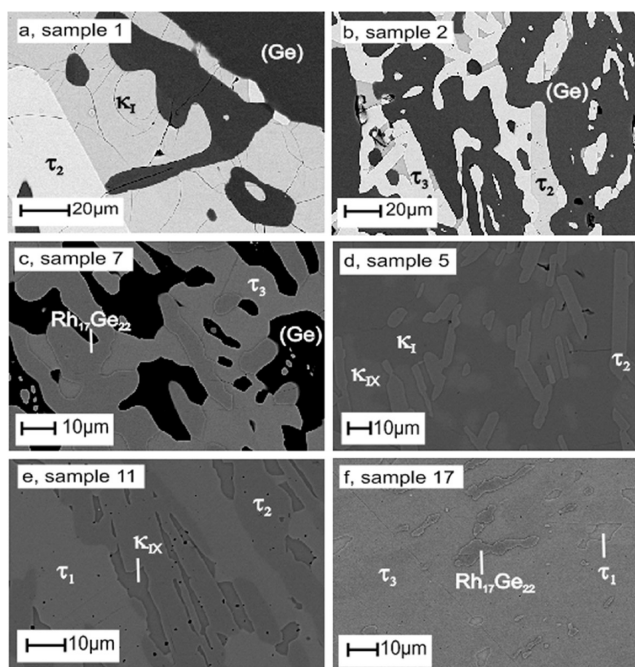

Figure 5. Micrographs (backscatter detector) of selected samples at 750 °C. The corresponding data are given in Table S2 (Supporting Information), and black circles in Figure 4 indicate the sample positions.

the existence of binary $Ba_8Ge_{43}\square_3$ is limited to a temperature interval from 770 to 810 °C,[9] also a lower limit of the solubility of Rh is expected and indicated in the isothermal section (Figure 4) but was not investigated. Rh stabilizes the clathrate I structure to 740 °C, where it decomposes in terms of a eutectoid reaction, $\kappa_I \Leftrightarrow (Ge) + \kappa_{IX} + \tau_2$, as determined by DTA measurements. Furthermore, EPMA data indicate a small solubility of Rh (0.5 atom %) in the clathrate IX phase. Similar to the results at 700 °C, a solubility range for $BaRh_{1-x}Ge_{3+x}$ with x_{max} = 0.25 was found. The crystallographic data and compositions of the compounds for the three-phase fields are presented in Table S2 (Supporting Information), and the respective micrographs are shown in Figure 5.

Careful analyses of various samples in the as-cast state as well as after annealing at 820, 800, 775, 770, 750, and 700 °C combined with DTA measurements revealed a rather complex reaction scheme between 830 and 700 °C, yielding nine four-phase reaction isotherms (see Figure 6). The corresponding liquidus and solidus projections are illustrated in Figure 7. In Figure 8, selected micrographs of different compositions are presented. Figure 8a documents a backscatter image of sample 7 annealed at 800 °C. The DTA measurement of this alloy shows the liquidus to appear slightly above 800 °C. From the micrograph, huge primary crystals (diameter >40 μm) of $Rh_{17}Ge_{22}$ can be seen. Those are surrounded by the peritectically formed τ_3 phase (P_1 in Figure 6), and finally the quenched liquid exhibits a fine eutectic structure containing three phases [$(Ge) + \kappa_I + \tau_3$; see also Figures 7 and 6, E_1]. From the as-cast sample 12, a cascade of several reactions can be examined (Figure 8b). The joint crystallization of τ_1 and τ_3 is followed by the peritectic formation of τ_2 (P_2 in Figure 6), and finally the crystallization field of the clathrate I phase is entered. In contrast to sample 4, the micrograph of sample 3 (Figure 8) shows that the (Ge) grains have much sharper boundaries because the sample position is still in the primary crystallization field of (Ge). Although clathrate I exhibits a very narrow crystallization field of only 2 °C,[17,18] this field is opening in the ternary system to a wide temperature and compositional range (Figure 7). A repre-

sentative micrograph of sample 4 clearly shows the large primary grains of κ_I. When the solidus (Figure 7), the isothermal section at 750 °C (Figure 4), and DTA are compared, two solid-state transition-type reactions are suggested around 760 °C (U_4 and U_5 in Figure 6). Because diffusion in solid-state reactions usually is dramatically reduced compared to reactions in which a liquid phase is involved, the EPMA data as well as PXRD patterns of samples 1 and 2 at 750 °C reveal the presence of small amounts of nonequilibrium phases τ_3 and κ_I, respectively.

4.3. Crystal Structures of the Ternary Phases.
4.3.1. Crystal Structure of the Clathrate I Phase. A suitable single crystal of the clathrate I phase was selected from a sample with the maximum Rh content annealed at 800 °C. Analysis of the measured X-ray intensity data revealed isotypism with the cubic crystal structure of K_4Ge_{23-x} (clathrate I type, space group $Pm\bar{3}n$). The occurrence of the necessary splitting of the 24k position (Ge2) in Ge-based type I clathrates indicates the presence of vacancies in the neighboring 6d position, as observed also in other clathrates.[24,25] As in the case of $Ba_8Rh_{1.2}Ge_{42.8}\square_{2.0}$, three different species (Ge, Rh, and $\square$) are occupying the 6d site, the Rh content was fixed during the structure refinement to an EPMA value of 1.2 Rh atoms/unit cell. The atomic displacement parameters (ADPs) of the other framework positions (16i and 24k) did not infer a mixed occupancy of Rh and Ge. Thus, all Rh atoms were placed in the 6d position, and the Ge content was allowed to vary during the refinement. The results presented in Table 2 [interatomic distances are listed in Table S3 (Supporting Information)] demonstrate sound correspondence of the vacancy amount in the 6d position with the occupancy of the Ge22 atoms in the 24k position at closer distances to the vacancies.

All attempts to allow anisotropic refinement of the ADPs at the 24k split position for the data set collected at 200 K led to unstable results, and therefore these positions were refined considering isotropic displacement parameters only. As summarized for several other clathrate I compounds, analysis of
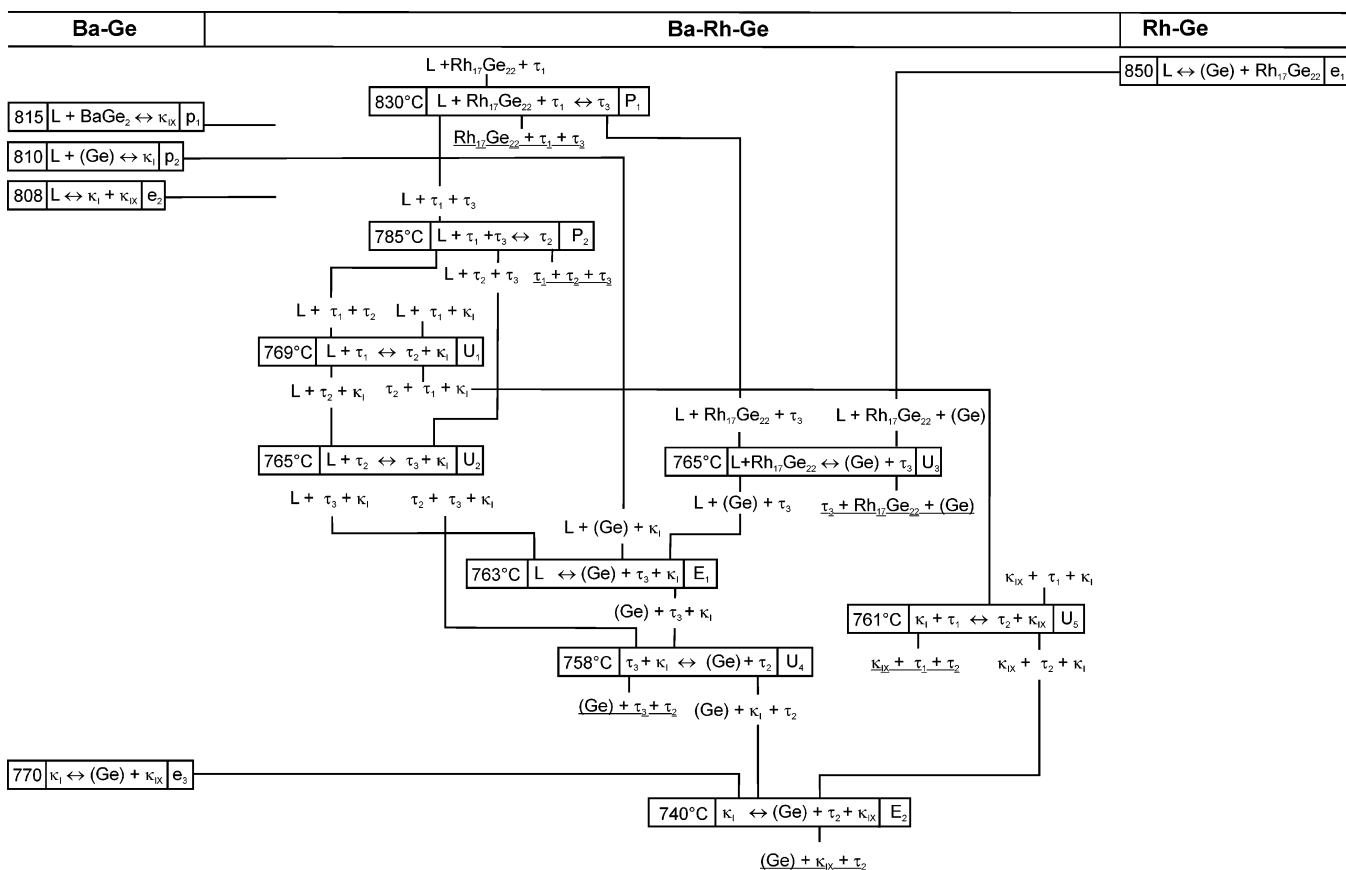
Figure 6. Reaction scheme (Schulz–Scheil diagram) for the Ge-rich part of the Ba–Rh–Ge system in the temperature range from 830 to 700 °C.
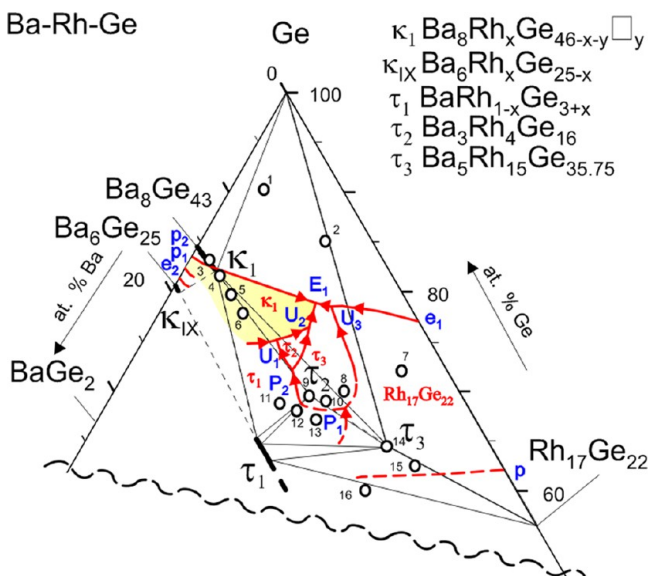

Figure 7. Liquidus and solidus projections of the Ge-rich part of the Ba–Rh–Ge system. The liquidus projection and primary crystallization fields of the phases are colored red, and the solidus, phases, and sample positions and numbers are colored black. The blue labels indicate the invariant reactions listed in Figure 6.
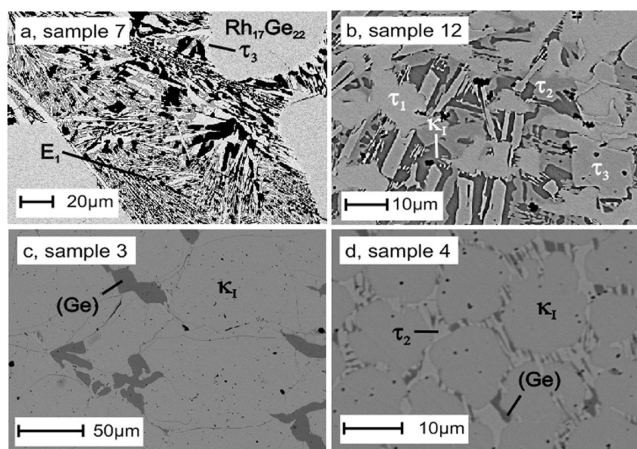

Figure 8. Selected micrographs (backscatter detector) of several samples (sample 7 was annealed at 800 °C for 1 week; all others are in the as-cast state after arc melting).

These values are well within the range of the values for Ba–Ge-based clathrate I compounds reported earlier.[4,26] The two Einstein temperatures originate from symmetry constraints (U_{11} is different from $U_{22} = U_{33}$ for the 6c site). The Debye temperature was calculated by taking into account only ADPs of the 16i position because this crystallographic site is the only framework position unaffected by mixed occupancy or splitting. Applying the calculation method tested earlier[26] to evaluate the thermal expansion coefficient α from the temperature-dependent lattice parameters $a(T)$, $\alpha_{100-300K} = 14.0 \times 10^{-6}$ K^{-1} was found. The results of these analyses are displayed in Figure 9.

temperature-dependent ADPs of guest and framework atoms allows conclusions on the lattice dynamics of the respective compound.[4] Applying least-squares fits to the equations given by Christensen[4] to extract Debye (θ_D) and Einstein (θ_E) temperatures resulted in $\theta_D = 245$ K, $\theta_{E,11} = 88$ K, and $\theta_{E,22,33} = 70$ K.

Table 2. Single-Crystal X-ray Data for Ba$_8$Rh$_{1.2}$Ge$_{42.8}$□$_{2.0}$ [Clathrate Type I, Mo Kα Radiation 2° ≤ 2Θ ≤ 70°; Anisotropic Displacement Parameters (in 10^{-2} nm^2)], Standardized with the Program *Structure Tidy*[39]

param/compd	300 K	200 K	100 K
space group	$Pm\bar{3}n$	$Pm\bar{3}n$	$Pm\bar{3}n$
composition from EPMA^a	Ba$_8$Rh$_{1.2}$Ge$_{42.6}$□$_{2.2}$	Ba$_8$Rh$_{1.2}$Ge$_{42.6}$□$_{2.2}$	Ba$_8$Rh$_{1.2}$Ge$_{42.6}$□$_{2.2}$
formula from refinement	Ba$_8$Rh$_{1.2}$Ge$_{42.8}$□$_{2.0}$	Ba$_8$Rh$_{1.2}$Ge$_{42.7}$□$_{2.1}$	Ba$_8$Rh$_{1.2}$Ge$_{42.7}$□$_{2.1}$
a [nm]	1.07081(3)	1.06926(3)	1.06779(3)
μ_{abs} [mm^{-1}]	33.66	33.81	33.95
ρ_x [g/cm^3]	6.043	6.069	6.094
reflns in refinement	341 ≥ 4σ(F_o) of 516	351 ≥ 4σ(F_o) of 514	372 ≥ 4σ(F_o) of 512
mosaicity	0.5	0.5	0.5
no. of variables	24	18	24
$R_F = \sum|F_o - F_c|/\sum F_o$	0.0279	0.0319	0.0273
R_{int}	0.0472	0.0441	0.0411
wR2	0.0448	0.0502	0.0409
GOF	1.170	1.162	1.114
extinction (Zachariasen)	0.000230	0.000095	0.000112
max; min residual density [e/Å^3]	1.22; −0.85	1.41; −1.50	1.97; −1.38
		Atom Parameters	
Ba1 in 2a (0, 0, 0); occ	1.00	1.00	1.00
$U_{11} = U_{22} = U_{33}$	0.0151(2)	0.0118(3)	0.0087(2)
Ba2 in 6c ($^1/_4$, 0, $^1/_2$); occ	1.00	1.00	1.00
U_{11}; $U_{22} = U_{33}$	0.0269(5); 0.0499(4)	0.0220(5); 0.0426(4)	0.0179(4); 0.0359(3)
M in 6d ($^1/_4$, $^1/_2$, 0); occ	0.2 Rh^b + 0.46(1) Ge + 0.34□	0.2Rh^b + 0.45(1)Ge + 0.35□	0.2Rh^b + 0.45(1)Ge + 0.35□
U_{11}; $U_{22} = U_{33}$	0.018(1); 0.0134(7)	0.013(1); 0.0101(7)	0.0116(8); 0.0074(5)
Ge1 in 16i (x, x, x) x; occ	0.18364(4); 1.00	0.18361(4); 1.00	0.18366(3); 1.00
$U_{11} = U_{22} = U_{33}$	0.0177(2)	0.0143(2)	0.0115(1)
Ge21 in 24k (0, y, z) y; z; occ	0.116(1); 0.309(1); 0.64(6)	0.1150(3); 0.3080(5); 0.59(2)	0.115(1); 0.3081(1); 0.58(6)
U_{11}; U_{22}; U_{33}	0.0162(8); 0.019(2), 0.016(2)	U_{iso} = 0.0131(6)^c	0.0081(7); 0.008(2); 0.013(2)
Ge22 in 24k (0, y, z) y; z; occ	0.133(2); 0.335(3); 0.36(6)	0.1321(6); 0.3330(8); 0.41(2)	0.131(1); 0.333(2); 0.42(6)
U_{11}; U_{22}; U_{33}	0.019(2); 0.022(3); 0.025(5)	U_{iso} = 0.0177(8)^c	0.011(1); 0.018(4); 0.012(2)

^{a}Ba content fixed to 8 atoms/unit cell. ^{b}Value fixed from EPMA data. ^{c}Anisotropic refinement unstable.
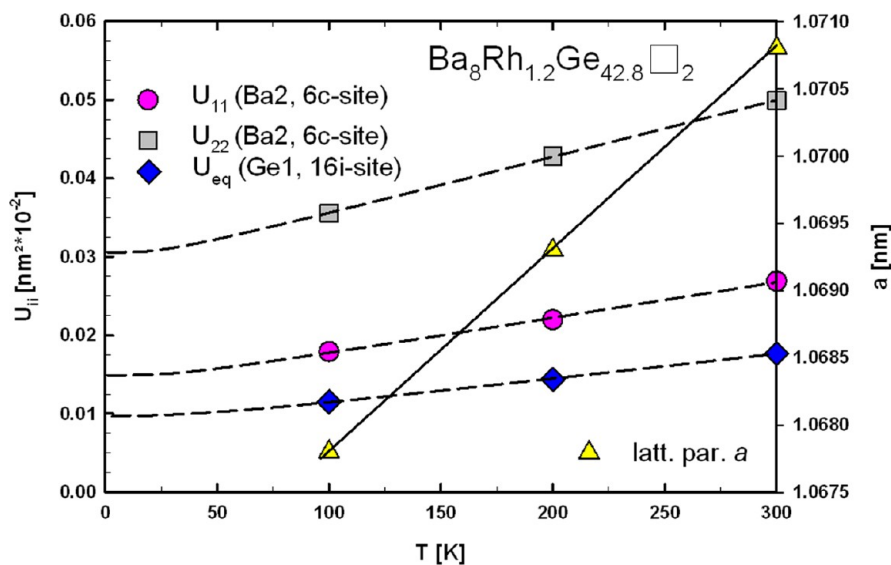
Figure 9. ADPs U_{ij} and lattice parameter a as a function of the temperature for Ba$_8$Rh$_{1.2}$Ge$_{42.8}$□$_{2.0}$.

4.3.2. Crystal Structure of the Phase τ_2-Ba$_3$Rh$_4$Ge$_{16}$. A suitable single crystal was selected from a sample with a nominal composition of τ_2 annealed at 775 °C for 1 week. Indexation of the single-crystal X-ray diffraction data revealed a tetragonal crystal lattice with a = 0.65643(2) nm and c = 2.20367(8) nm. Analysis of the systematic extinctions prompted the extinction symbol $I---$ with the centrosymmetric body-centered-cubic

space group $I4/mmm$ with highest symmetry. The structure was solved by applying direct methods and refinement of seven atom sites with anisotropic ADPs converged to R_F = 0.0273 and a residual electron density of <2 e/Å^3. Detailed results are listed in Table 3 and atom parameters are given in Table 4. [Interatomic distances are listed in Table S4 (Supporting Information)]. Ba atoms are located at the 2a and 4d positions,

Table 3. X-ray Single-Crystal Data for $Ba_3Rh_4Ge_{16}$ and $Ba_5Rh_{15}Ge_{36-x}$ ($x = 0.25$); (Mo Kα Radiation)

| param/compd	$Ba_3Rh_4Ge_{16}$	$Ba_5Rh_{15}Ge_{35.75}$
space group	$I\,4/mmm$ (No. 139)	$Fddd$ (No. 70)
structure type	$Ba_3Rh_4Ge_{16}$	$Ba_5Rh_{15}Ge_{35.75}$
composition from EPMA	$Ba_{13.0}Rh_{18.0}Ge_{69.0}$	$Ba_{8.9}Rh_{27.2}Ge_{63.9}$
composition from refinement	$Ba_{13.0}Rh_{17.4}Ge_{69.6}$	$Ba_{9.0}Rh_{26.9}Ge_{64.1}$
formula from refinement	$Ba_3Rh_4Ge_{16}$	$Ba_5Rh_{15}Ge_{35.73}$
a, b, c [nm]	0.65643(2), −, 2.20367(8)	0.84750(2), 1.4725(2), 6.644(3)
μ_{abs} [mm^{-1}]	34.33	30.75
ρ_x [g/cm^3]	6.943	6.705
reflns in refinement	$507 \geq 4\sigma(F_o)$ of 672	$3066 \geq 4\sigma(F_o)$ of 4563
mosaicity	0.5	0.5
no. of variables	26	139
$R_F = \sum|F_o - F_c|/\sum F_o$	0.0273	0.0340
R_{int}	0.0681	0.0819
wR2	0.0770	0.0554
GOF	0.994	1.014
extinction (Zachariasen)	0.000085	0
max; min residual density [e/Å^3]	1.99; −1.34	2.25; −2.00

Table 4. Atom Parameters for $Ba_3Rh_4Ge_{16}$ Standardized with Program *Structure Tidy*[39] [Anisotropic Displacement Parameters (in 10^{-2} nm^2)]

Atom Parameters	
Ge1 in 16m (x, x, z)	0.24358(8); 0.12878(3)
$U_{11} = U_{22}$; U_{33}	0.0136(2); 0.0142(3)
Ge2 in 8j ($x, ^1/_2, 0$)	0.2284(1)
U_{11}; U_{22}; U_{33}	0.0116(4); 0.0125(4); 0.0118(4)
Ge3 in 4e (0, 0, z)	0.19687(6)
$U_{11} = U_{22}$; U_{33}	0.0156(4); 0.0145(7)
Ge4 in 4e (0, 0, z)	0.31070(7)
$U_{11} = U_{22}$; U_{33}	0.0171(4); 0.0155(7)
Rh in 8g (0, $^1/_2, z$)	0.08871(3)
U_{11}; U_{22}; U_{33}	0.0082(3); 0.0083(3); 0.0116(3)
Ba2 in 4d (0, $^1/_2, ^1/_4$)	
$U_{11} = U_{22}$; U_{33}	0.0118(2); 0.0113(3)
Ba1 in 2a (0, 0, 0)	
$U_{11} = U_{22}$; U_{33}	0.0129(3); 0.0143(5)

Rh occupies the 8g site, and Ge atoms adopt the 16m, 8j, and two 4e sites. During the refinement, full ordering and full occupancy of all sites was confirmed. The composition extracted from the single-crystal analysis is in fair agreement with the EPMA results (see Table 3).

The unit cell dimensions exhibit a close relation to the $BaAl_4$ structure type, crystallizing in the same space group symmetry: $a = \sim\sqrt{2}a_{BaAl_4}$ and $c = \sim2c_{BaAl_4}$. The 4-fold cell volume is caused by occupation of the voids and some significant shifts of the atomic sites with respect to the $BaAl_4$ structure type. The positions of the Ba atoms are split but principally maintained; the Al1 site splits into the Ge1 and Ge2 sites. Half of the Al2 sites are occupied by the Ge3 and Ge4 atoms, while the other half is shifted along [001] and occupied by Rh atoms, which

allows a new site for the Ge2 atoms and significantly different coordination figures around the two Ba sites. The coordination polyhedron of the Ba2 atoms in the 4d site with coordination number 18 is akin to the coordination polyhedron of Ba in the $BaAl_4$ structure; only a slight distortion is observed as the Al atoms at the 4e site of $BaAl_4$ are replaced by two 4e sites, both occupied by Ge atoms. In addition, the Rh site is located on the top and bottom of the polyhedron, forming tetragons with the Ge1 atoms (see Figure 10). Analysis of the Voronoi
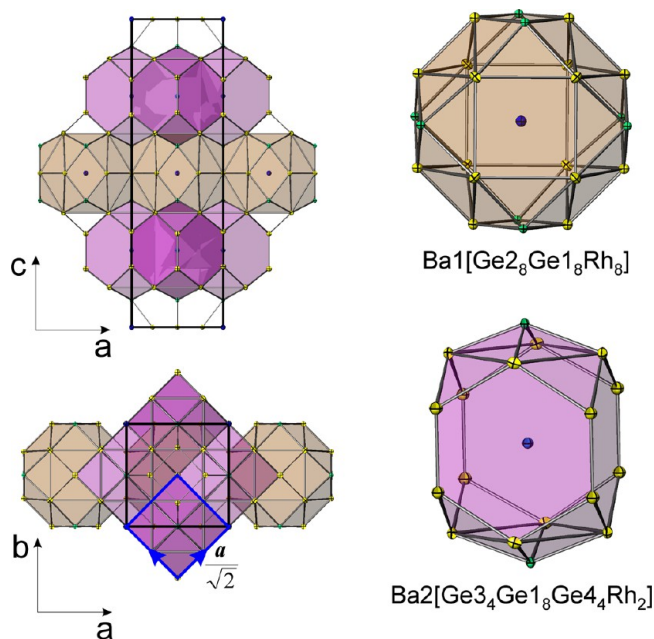
Figure 10. Crystal structure of τ_2-$Ba_3Rh_4Ge_{16}$. Ba atoms are colored blue, Rh green, and Ge yellow. In the projection on the (001) plane, the respective unit cell of the $BaAl_4$ type is outlined by blue lines.

coordination polyhedron of Ba1 using the program *DIDO95*[27] defined 24 neighboring atoms with areas contributing to the Dirichlet domain (Ba1[Ge2$_8$Ge1$_8$Rh$_8$]; Figure 10). Infinite and alternating layers of polyhedra around the Ba1 and Ba2 atoms describe the whole crystal structure: the polyhedra around the Ba2 atoms are connected via hexagons to other four neighboring and symmetry-equivalent polyhedra, and also the polyhedra around the Ba1 atoms are within a layer connected via tetragonal faces to four neighbors. The crystal structure is built up by an alternation of those different layers, which are sharing trigonal faces and leaving tetragonal-pyramidal cavities (see Figure 10). The search for an identical structure type (Pearson symbol: tI46) in Pearson's Crystal Data[28] prompted no results, defining $Ba_3Rh_4Ge_{16}$ as a unique structure type.

4.3.3. Crystal Structure of the Phase τ_3-$Ba_5Rh_{15}Ge_{36-x}$. A suitable single-crystal fragment of the phase was selected from an alloy [sample 15; Ba, 7.5 atom %; Rh, 30 atom %; Ge, 62.5 atom%; see also Table S1 (Supporting Information)] annealed at 800 °C. X-ray diffraction data were successfully indexed on the basis of a large orthorhombic unit cell exhibiting systematic extinctions consistent with face-centering and lattice dimensions of $a = 0.84570(2)$ nm, $b = 1.4725(2)$ nm, and $c = 6.644(3)$ nm. Symmetry analysis revealed space group $Fddd$ as the only possible space group from the extinction rules. Direct methods allowed the assignment of the three different species (Ba, Rh, and Ge) to the respective crystallographic positions, resulting in reasonable inter-atomic distances [see Tables 3, 5, and S5 (Supporting Information)]

Table 5. Atom Parameters for $Ba_5Rh_{15}Ge_{36-x}$ ($x = 0.25$) Standardized with program *Structure Tidy*[39] [Anisotropic Displacement Parameters (in 10^{-2} nm^2)]

Atom Parameters	
Ge1a in 32h (x, y, z)	0.0059(8); 0.0064(8); 0.20741(3)
occ, U_{iso}	0.55(3); 0.0154(6)
Ge1b in 32h (x, y, z)	0.032(1); 0.033(1); 0.20757(6)
occ, U_{iso}	0.15(1); 0.011(2)
Ge1c in 32h (x, y, z)	0.9887(9); 0.9883(9); 0.20720(5)
occ, U_{iso}	0.30(1); 0.015(1)
Ge2 in 32h (x, y, z)	0.00394(8); 0.41845(4); 0.06750(1)
occ	0.933(2)
U_{11}; U_{22}; U_{33}	0.0194(4); 0.0165(3); 0.0231(4)
Ge3 in 32h (x, y, z)	0.10680(7); 0.34855(4); 0.10461(1)
U_{11}; U_{22}; U_{33}	0.0142(2); 0.0164(3); 0.0166(3)
Ge4 in 32h (x, y, z)	0.11312(7); 0.45405(4); 0.02797(1)
U_{11}; U_{22}; U_{33}	0.0173(3); 0.0150(3); 0.0219(9)
Ge5 in 32h (x, y, z)	0.22289(7); 0.26373(4); 0.35229(1)
U_{11}; U_{22}; U_{33}	0.0173(3); 0.0151(3); 0.0177(3)
Ge6 in 32h (x, y, z)	0.26412(7); 0.17143(4); 0.07278(1)
U_{11}; U_{22}; U_{33}	0.0137(3); 0.0136(3); 0.0228(3)
Ge7 in 32h (x, y, z)	0.35578(7); 0.20218(4); 0.02998(1)
U_{11}; U_{22}; U_{33}	0.0164(3); 0.0147(3); 0.0216(3)
Ge8 in 32h (x, y, z)	0.45174(7); 0.00667(4); 0.10567(1)
U_{11}; U_{22}; U_{33}	0.0148(3); 0.0153(3); 0.0170(3)
Ge9 in 16g ($1/8, 1/8, z$)	0.00038(1)
U_{11}; U_{22}; U_{33}	0.0129(4); 0.0163(4); 0.0180(4)
Ge10 in 16g ($1/8, 1/8, z$)	0.49912(1)
U_{11}; U_{22}; U_{33}	0.0137(4); 0.0163(4); 0.0170(4)
Rh1 in 32h (x, y, z)	0.00120(5); 0.00377(3); 0.17159(1)
U_{11}; U_{22}; U_{33}	0.0130(2); 0.0132(2); 0.0132(2)
Rh2 in 32h (x, y, z)	0.15044(5); 0.29942(3); 0.01423(1)
U_{11}; U_{22}; U_{33}	0.0130(2); 0.0147(2); 0.0142(2)
Rh3 in 32h (x, y, z)	0.40000(5); 0.05091(3); 0.01407(1)
U_{11}; U_{22}; U_{33}	0.0123(2); 0.0147(2); 0.0142(2)
Rh4 in 16g ($1/8, 1/8, z$)	0.36959(1)
U_{11}; U_{22}; U_{33}	0.0124(3); 0.0153(3); 0.0154(3)
Rh5 in 8a ($1/8, 1/8, 1/8$)	
U_{11}; U_{22}; U_{33}	0.0178(4); 0.0122(4); 0.0209(4)
Ba1 in 16g ($1/8, 1/8, z$)	0.31154(1)
U_{11}; U_{22}; U_{33}	0.0177(2); 0.0143(2); 0.0197(2)
Ba2 in 16g ($1/8, 1/8, z$)	0.56110(1)
U_{11}; U_{22}; U_{33}	0.0157(2); 0.0165(2); 0.0204(2)
Ba3 in 8a ($1/8, 1/8, 1/8$)	
U_{11}; U_{22}; U_{33}	0.0202(4); 0.0190(3); 0.0199(3)

and sound agreement of the refined composition $Ba_{9.0}Rh_{26.9}Ge_{64.1}$ with the EPMA value of $Ba_{8.9}Rh_{27.2}Ge_{63.9}$.

Whereas refinement of the occupancy for Ge2 resulted in a slight deficiency (occ = 0.93), the same attempt failed for Ge1 located in the 32h position with $x = 0.2528$, $y = 0.2531$, and $z = 0.2929$. When isotropic ADPs were applied, two rather high peaks of ~15 e/Å^3 were detected by difference Fourier synthesis at a distance closer than 0.05 nm to the respective atom position. A detailed inspection of the electron density at this

site via a difference Fourier calculation by removing the Ge1 atom revealed an elliptically shaped electron density in the two-dimensional plot parallel to the (001) plane (Figure 11). Although the three-dimensional image does not provide a clear conclusion on the splitting of this site, the improvement in the R values after splitting into two or three separate positions is significantly large (from 0.07 to 0.034 for R_F in both cases). The splitting into a 2-fold site with isotropic ADPs leaves a small electron density at a distance of 0.058 nm to the Ge position with higher occupation (69%) but with no correlation to the vacancy amount of Ge2. In contrast to this observation, a 3-fold splitting results in reasonable U_{iso} values, and even without restraining the sum of the occupancies to unity, it results in a completely filled 32-fold site, indicating that the whole electron density in this particular part of the unit cell is covered, allowing three atom positions. Moreover, the distribution of the occupancy [Table 5 and Figure S1 (Supporting Information)] over the three sites correlates with the vacancy amount at the Ge2 site. The sites Ge1a/b/c are located inside an infinite channel formed by Ge pentagons and Rh triangles [see Figure S1 (Supporting Information)]. Ge1a is located directly in the center of the triangle formed by Rh atoms, and all bonding distances are rather short compared to the other Ge–Rh distances in this structure [see Table S5 (Supporting Information)]. It seems that, whenever one of the Ge2 sites remains vacant (occ. 7%), the two Ge1 atoms close to this vacancy are shifted further away to the Ge1b site (occ. 15%), closer to the pentagonal plane formed by two Ge6, two Ge7, and one Ge9, respectively [Figure S1 (Supporting Information)]. In order to avoid the short distances to the Rh atoms, the third split site (Ge1c position) is released to the other side of the triangle closer to the pentagonal face formed by two Ge2, two Ge4, and one Ge10 [see Figure S1 (Supporting Information)].

The final refinement with anisotropic ADPs (except for Ge1a/b/c) converged to $R_F = 0.0340$ and a residual electron density of <2.3 e/Å^3. Detailed results are listed in Table 3. There are three distinct positions for Ba atoms present in the crystal structure, and all of their coordination polyhedra are characterized by distorted faces (see Figure 12). Although the Voronoi polyhedra of Ba1 and Ba2 look similar, a detailed analysis of the Dirichlet domains using the program *DIDO95*[27] revealed a slight difference in the coordination number: whereas Ba1 has 20 neighbors [neglecting two Ba2 atoms, which are contributing an area of only 1% to the domain (see the Supporting Information)], for Ba2, only 19 neighbors were identified [also neglecting two Ba1 atoms, which are contributing a small area (1.1%) to the domain; see Table S5 (Supporting Information) and Figure 12]. The entire structure is built up by blocks, which are formed by layers of polyhedra around the Ba1 and Ba2 atoms. They are alternately linked to each other by sharing pentagons. Between two of those layers the polyhedra around the Ba3 atoms are located, which are not connected via any face or atom but are linked to four neighbors via bonds to two Rh4 and two Rh5 atoms. The Ba3 polyhedra are linked to four Ba1 and four Ba2 polyhedra, two of each at the bottom and top sharing tetragons. The layers of Ba1/Ba2 polyhedra are rotated against each other by 60°. The four blocks per unit cell are shifted and rotated according to the symmetry operators of the space group *Fddd*. A search for the structure type (Pearson symbol: oF448) in Pearson's Crystal Data[28] prompted no results with these lattice parameters, crystal symmetry, and Wyckoff sequence, suggesting $Ba_5Rh_{15}Ge_{35.75}$ to be a unique structure type.

4.4. DFT Results. The energies of formation of $Ba_8Rh_xGe_{46-x}$ for various values of $x = 0-6$ were derived from the DFT
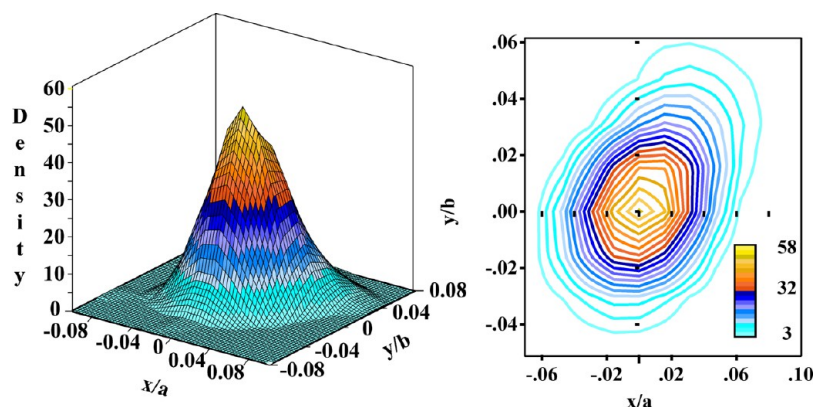
Figure 11. Three- and two-dimensional difference Fourier maps of the Ge1 atom parallel to the (001) plane at $z/c = 0.2074$ of τ_3-$Ba_5Rh_{15}Ge_{35.75}$.
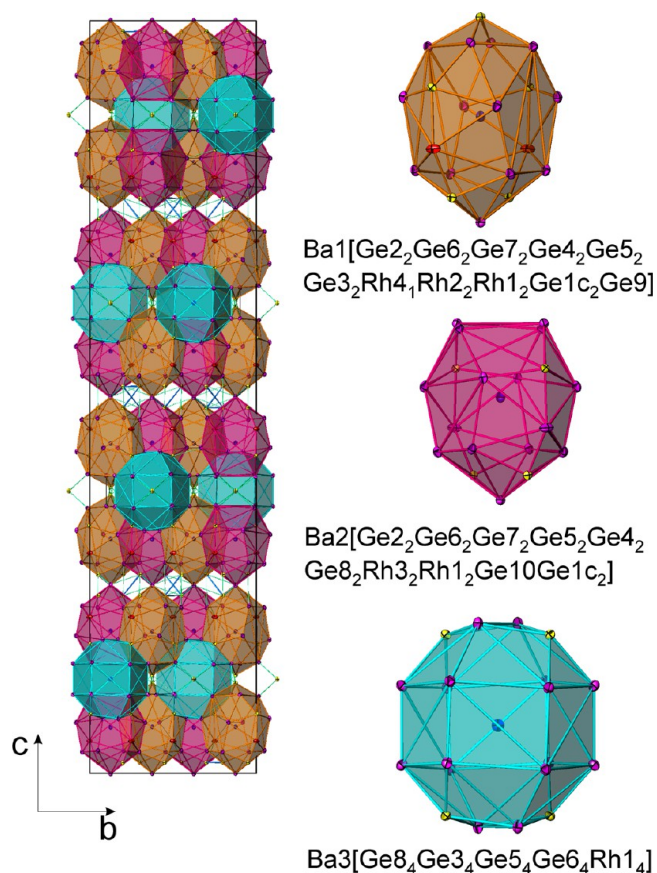

$Ba1[Ge2_2Ge6_2Ge7_2Ge4_2Ge5_2$
$Ge3_2Rh4_1Rh2_2Rh1_2Ge1c_2Ge9]$

$Ba2[Ge2_2Ge6_2Ge7_2Ge5_2Ge4_2$
$Ge8_2Rh3_2Rh1_2Ge10Ge1c_2]$

$Ba3[Ge8_4Ge3_4Ge5_4Ge6_4Rh1_4]$

Figure 12. Crystal structure of τ_3-$Ba_5Rh_{15}Ge_{35.75}$ and the coordination polyhedra for the three different Ba positions. Ba atoms are colored blue and Rh yellow, and Ge atoms are colored pink, red [Ge1a (Ge1b/c not plotted)], and orange (Ge2).
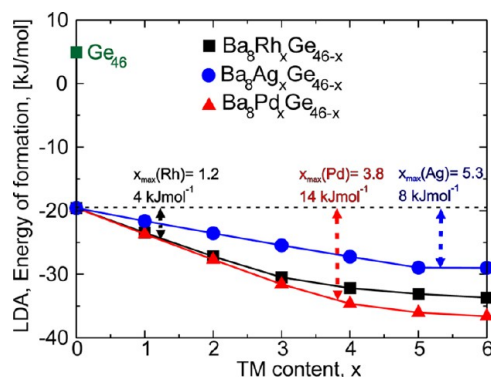

Figure 13. DFT-derived enthalpy of formation for $Ba_8M_xGe_{46-x}$ (M = Rh, Pd, Ag; $x = 0-6$) and for the Ge_{46} framework. The information on the maximum solubility for $Ba_8Pd_xGe_{46-x}$ and $Ba_8Ag_xGe_{46-x}$ are taken from refs 40 and 29, respectively.

calculations at zero pressure, which are shown in Figure 13. As mentioned in our previous studies, experimentally the dopants are randomly distributed over the 6d site. For the DFT calculations, the doping atoms have to be placed on specific sites within the unit cell, which, in general, causes changes of the lattice symmetry and cell shape. Therefore, to be consistent with the experiment, a cubic unit cell was enforced for all calculations. More details on the types of calculations are given in refs 29 and 30. For comparison, the enthalpies of formation (ΔH) for $Ba_8Pd_xGe_{46-x}$ and $Ba_8Ag_xGe_{46-x}$[29] which were studied recently, are also shown in Figure 13. The incorporation of Ag

into the Ge framework stabilizes the clathrate I compound, as evidenced by a decrease of ΔH of −10 kJ/mol for $x = 0-5$ (Figure 13). Further enrichment of Ag up to $Ba_8Ag_6Ge_{40}$ does not further decrease ΔH, which is in line with the solubility limits found in the experiments. In contrast to this, alloying of Rh and Pd has much more pronounced effects on the stabilization of $Ba_8M_xGe_{46-x}$. The formation energies for both compounds decrease monotonically. These unequal behaviors are attributed to the difference in pd bonding between closed and open d shell elements, which were discussed in our previous work.[31]

DOSs for $Ba_8Rh_xGe_{46-x}$ (with $x = 1-6$) are shown in Figure 14. Significant changes by doping with Rh can be observed. The gap, clearly present in Ba_8Ge_{46}, shrinks more and more by substituting Ge by Rh, implying strong hybridization between the two framework-forming species. For the hypothetical compound $Ba_8Rh_1Ge_{45}$, a peak emerges in the gap. As the doping of Rh increases, the peak extends and gradually mixes with framework states, which leads to small pseudogaps at about −0.1 eV in $Ba_8Rh_3Ge_{43}$ and at about 0.3 eV in $Ba_8Rh_4Ge_{42}$, respectively. Upon further substitution of up to six Rh/unit cell, a gap appears. In this case, it is located above the Fermi level.
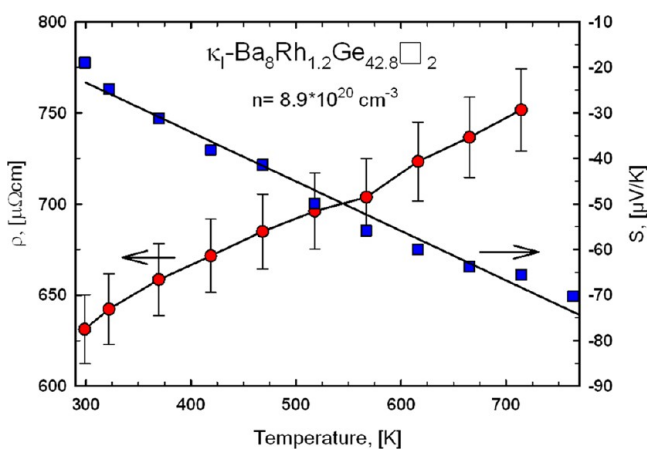
Our previous studies[29−31] revealed that the location of E_F plays an important role in understanding the Seebeck coefficient. For $Ba_8M_xGe(Si)_{46-x}$, a simple electron-counting rule was proposed to define the critical composition, for which the Fermi energy falls into the gap, i.e., $x_{gap} = 16/(4 - n)$, with n being the valency of the dopant. This rule has been successfully applied to

939

dx.doi.org/10.1021/ic302139r | *Inorg. Chem.* 2013, 52, 931−943
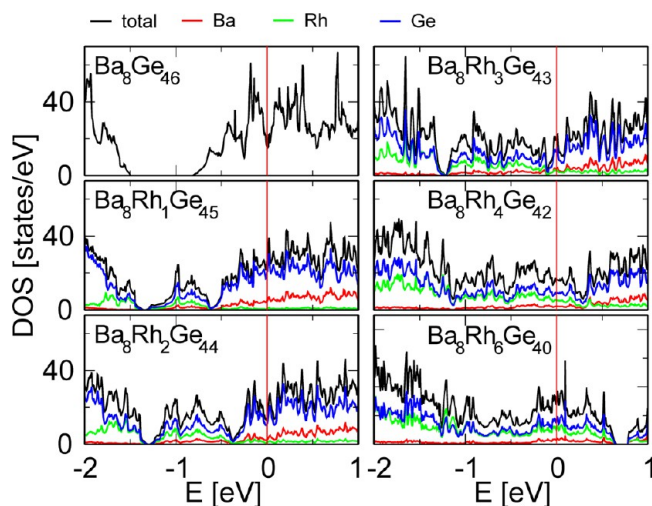
Figure 14. DFT-derived DOSs for $Ba_8Rh_xGe_{46-x}$ (x = 0−6). Energy scale with respect to the Fermi energy.

$Ba_8M_xGe(Si)_{46-x}$ (M = Cu, Ag, Au, Pd, and Ni). Assuming a formal valency of −1 for Rh results in x_{gap} = 3.2. This value of −1 derives from the electron configuration of the outer shell (Rh, $4d^8 5s$; Ge, $3d^{10} 4s^2 4p^2$). In order to arrive at the isovalent composition, which corresponds to the Sn configuration ($4d^{10} 5s^2 5p^2$), Rh requires five additional electrons. Because the valency, n, of Ge is 4, the five less electrons for Rh results in n = −1. Please note that each vacancy (□) corresponds to a valency n = 0 because no electrons are provided. In Figure 14, a narrow valley in the DOS of $Ba_8Rh_3Ge_{43}$ at about −0.1 eV is observed, but a real gap is absent. Experimental samples are $Ba_8Rh_xGe_{46-x-y}□_y$ with a solubility of Rh up to about 1.2. This indicates the importance of vacancies in the stability and bonding of the clathrate I structure. If one assumes that each vacancy compensates four electrons, x_{gap} = 1.6 is obtained for a semiconducting charge-balanced compound $Ba_8Rh_xGe_{46-x-y}□_y$, which is much closer to the experimental value for the solubility of Rh in the present system.

4.5. Physical Properties. *4.5.1. Physical Properties of the Clathrate I $Ba_8Rh_{1.2}Ge_{42.8}□_{2.0}$.* The temperature dependence of the electrical resistivity (ρ) as well as of the Seebeck coefficient (S) of a clathrate sample with a maximum Rh content of 1.2 atoms/unit cell is plotted in Figure 15. PXRD and EPMA

data for this sample prompted minor impurities of Ge (<4 wt %) and $τ_2$ (<2 wt %). Both electrical resistivity and the Seebeck coefficient reveal an almost linear temperature dependence typical for metallic-like systems, which is expected for $Ba_8Rh_{1.2}Ge_{42.8}□_{2.0}$ in terms of the Zintl formalism. The charge-balanced composition is $Ba_8Rh_{3.2}Ge_{42.8}$ (Rh compensates for $5e^-$ in the tetrahedrally bonded Ge framework), but because the Rh solubility limit at 800 °C is 1.2 and each vacancy is considered to compensate for $4e^-$, there remain still $2e^-$ of the total $16e^-$ supplied by the Ba atoms (eight Ba^{2+}).

In order to get a rough estimation of the charge carrier density, Mott's formula 1 was employed, giving the diffusion thermopower in terms of a free electron model[32]

$$S_d(T > θ_D) = \frac{π^2 k_B^2 2 m_e}{e\hbar^2 (3nπ^2)^{2/3}} T \tag{1}$$

where m_e is the electron mass and e is the carrier charge. A linear fit to S(T) resulted in a charge carrier density n of $\sim10^{21}$ cm^{-3}. This value is in rather sound agreement with 1.6×10^{21} cm^{-3}, resulting from a simple calculation assuming that the two uncompensated electrons/unit cell [a = 10.6932(2) nm] for $Ba_8Rh_{1.2}Ge_{42.8}□_{2.0}$ serve as charge carriers.

4.5.2. Physical Properties of $τ_1$-BaRhGe$_3$. An as-cast sample was used for electrical resistivity measurements. EPMA analysis consistent with the Rietveld refinement proved BaRhGe$_3$ as the main phase with traces of BaRh$_2$Ge$_2$ (<3%; ThCr$_2$Si$_2$ type[33]). Below 300 K, BaRhGe$_3$ exhibits a temperature dependence of the electrical resistivity typically observed for metallic compounds (see Figure 16). Down to 1.8 K, no superconducting transition is
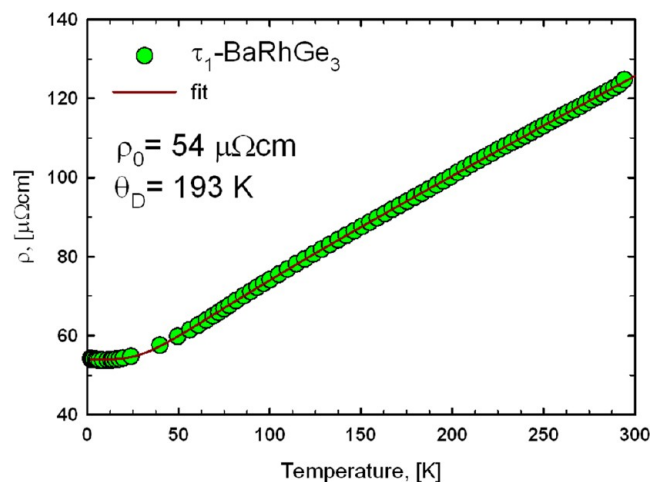
Figure 16. Electrical resistivity ρ as a function of the temperature for $τ_1$-BaRhGe$_3$. The solid line displays the results of a least-squares fit to the Bloch−Grüneisen model.

Figure 15. Electrical resistivity ρ and Seebeck coefficient S of $κ_I$-$Ba_8Rh_{1.2}Ge_{42.8}□_{2.0}$ as a function of the temperature. The solid black line represents a linear fit to the S data.

observed and ρ(T) can be described up to 300 K fairly well using the Bloch−Grüneisen model ($ρ_{BG}$ in eq 2) for metals (red solid line in Figure 16), resulting in a residual resistivity $ρ_0$ = 54 μΩ cm and a Debye temperature $θ_D$ = 193 K.

4.5.3. Physical Properties of $τ_2$-Ba$_3$Rh$_4$Ge$_{16}$. The electrical resistivity of Ba$_3$Rh$_4$Ge$_{16}$ was measured in the temperature range from 300 mK to 300 K. The resistivity vanishes at T_C = 6.5 K, indicating a transition into a superconducting state. Above T_C, the resistivity data exhibit a simple metallic temperature dependence. The residual resistivity ratio from room temperature to 6.5 K is around 6.2, referring to a good sample quality. The s−d

scattering on Rh atoms in the sense of Mott and Jones has been taken into account but does not seem to possess any significant contribution. However, the results can be accounted for in terms of the parallel resistor model:[34]

$$\frac{1}{\rho(T)} = \frac{1}{\rho_{BG}(T)} + \frac{1}{\rho_{max}}$$

$$\text{with } \rho_{BG}(T) = \rho_0 + R\left(\frac{T}{\theta_D}\right)^5$$

$$\int_0^{\theta_D/T} \frac{z^5 \, dz}{(e^z - 1)(1 - e^{-z})} \tag{2}$$

In this model, ρ_{BG} is the Bloch–Grüneisen term and ρ_{max} the saturation resistivity. A least-squares fit reveals a residual resistivity of ∼23 $\mu\Omega$ cm and a saturation resistivity of ∼321 $\mu\Omega$ cm (shown as a solid line in Figure 17). As a result, a Debye tem-
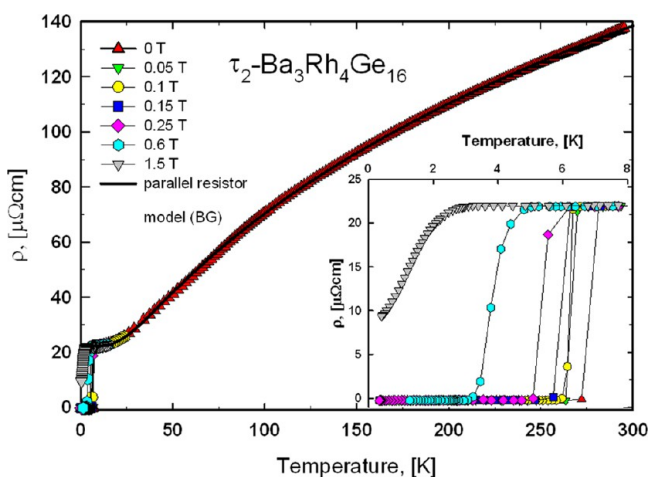

Figure 17. Electrical resistivity ρ as a function of the temperature and magnetic field (in Tesla) for τ_2-Ba$_3$Rh$_4$Ge$_{16}$. The solid line represents a least-squares fit to the parallel resistor model. The inset shows low-temperature details of the superconducting transition.

perature of ∼145 K was determined. Employing the empirical model of McMillan leads to an electron–phonon coupling constant $\lambda_{ep} \approx 0.9$, indicating a value beyond the BCS weak-coupling limit. Resistivity measurements were carried out in various external fields also. With increasing magnetic field, the transition temperature shifts to lower values until the super-conducting state is completely suppressed at 1.5 T in the tem-perature range available (inset Figure 17). A commonly used 90/10 technique, i.e., the midpoint between 90% of ρ_0 and 10% of ρ_0, determines the superconducting transition temperature. Results are collected in Figure 18. The initial slope of the upper critical field is derived as

$$-\frac{\partial H_{c2}}{\partial T}\bigg|_{T=T_C} = 0.253 \tag{3}$$

The model by Werthamer et al.[35] (WHH) is used to describe the temperature dependence of the upper critical field (red solid line in Figure 18). This model takes into account the spin–orbit scattering (λ_{so}), causing the electron spin to no longer be a good quantum number, and the depairing mechanism due to Zeeman splitting, called the Pauli limiting (PL). Quantitatively, two parameters guide this model, i.e., the
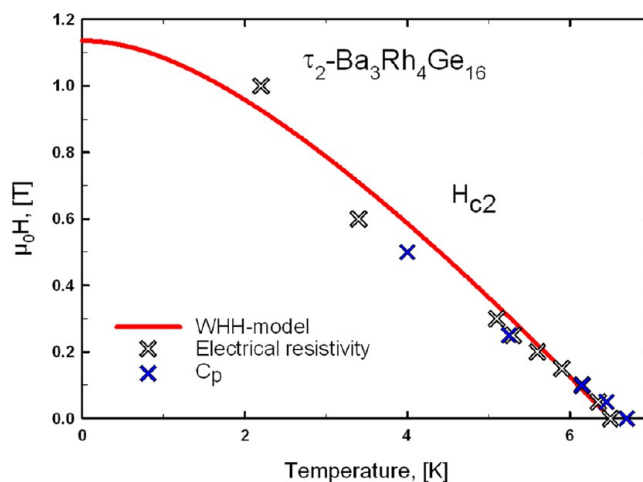
Figure 18. Temperature-dependent upper critical magnetic field H_{c2} of τ_2-Ba$_3$Rh$_4$Ge$_{16}$. The solid line is a fit according to the WHH model (see the text).

Maki parameter[36] and the spin–orbit interaction constant. The Maki parameter can be estimated from

$$\alpha = 5.35*10^{-5}*H_{c2}'*10000 = 0.135 \tag{4}$$

This small value hints to a rather limited influence of the PL and, therefore, the establishment of orbital depairing to play the essential role in this material. The WHH model predicts an upper critical field of 1.14 T. An alternative route to derive α follows from[35]

$$\alpha = 3\frac{e^2 \hbar \gamma \rho_0}{2m_e \pi^2 k_B} = 0.139 \tag{5}$$

where e is the electron charge, m_e the electron mass, γ the Sommerfeld value, and ρ_0 the residual resistivity. The Maki parameter obtained from eq 5 coincides very well with that derived from eq 4. Details on the superconducting state of τ_2-Ba$_3$Rh$_4$Ge$_{16}$ will be presented in a future publication.

Heat Capacity of τ_2-Ba$_3$Rh$_4$Ge$_{16}$. Specific heat mea-surements were performed from 2 to 80 K in magnetic fields from 0 to 2 T, and the results are displayed as C_p/T versus T in Figure 19. In zero fields, a sharp second-order transition occurs
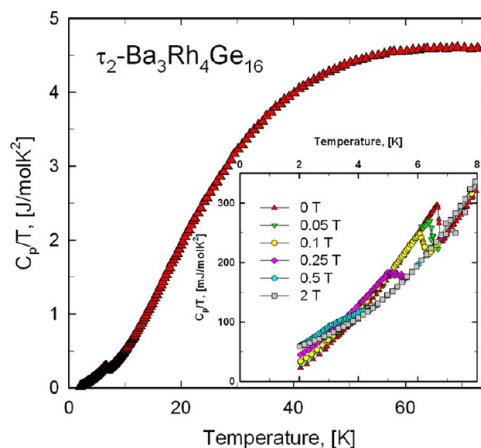
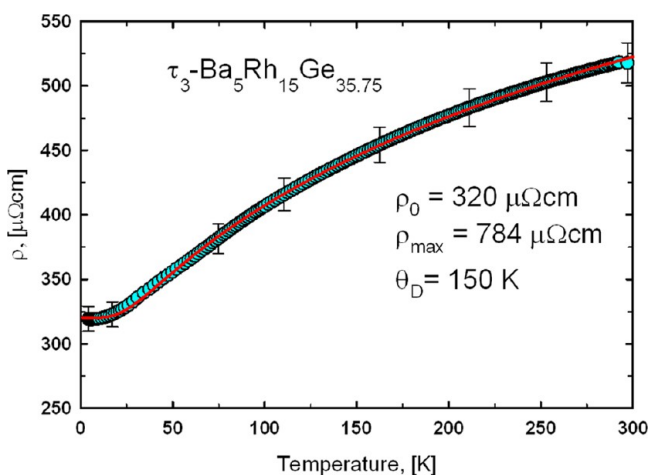**Figure 19.** C_p/T as a function of the temperature and magnetic field for τ_2-Ba$_3$Rh$_4$Ge$_{16}$. The inset shows a detailed view of the jump at the critical temperature (T_C).

at around 6.7 K, confirming the superconducting transition. In conjunction with the heat capacity anomaly at $T = T_C$, bulk superconductivity can be concluded. The electronic Sommerfeld coefficient (γ) is about 80 mJ/mol·K^2. The H_{c2} behavior extracted from the field dependence of the superconducting specific heat anomaly fits well to the results obtained from electrical resistivity measurements. The ratio of the superconducting specific heat jump to the normal state heat capacity γT_C yields

$$\frac{\Delta C_p(T_C)}{\gamma T_C} \approx 1.38 \tag{6}$$

which is close to the BCS value of 1.43. The inset of Figure 19 shows the field dependence of the jump at T_C.

   4.5.4. Physical Properties of τ_3-Ba$_5$Rh$_{15}$Ge$_{35.75}$. The electrical resistivity from 4 to 300 K is plotted in Figure 20.

Figure 20. Electrical resistivity ρ as a function of the temperature for τ_3-Ba$_5$Rh$_{15}$Ge$_{35.75}$. The solid line represents a least-squares fit to the model described in the text.

The temperature dependence is metallic-like, and in contrast to Ba$_3$Rh$_4$Ge$_{16}$, no superconductor transition was observed to 4.1 K. At elevated temperatures, the slope of the electrical resistivity significantly deviates from the simple linear temperature dependence and can be well described by applying the parallel resistor model (eq 2). Using this model to fit the data, residual resistivity $\rho_0 = 320$ $\mu\Omega$ cm, saturation resistivity $\rho_{max} = 784$ $\mu\Omega$ cm, and Debye temperature $\theta_D = 150$ K were extracted. Measuring the Seebeck coefficient at room temperature revealed electrons to be the main charge carriers and that the value of -6 μV/K is relatively small, as expected for metals and intermetallic compounds.

5. CONCLUSIONS

Although the solubility of Rh is rather limited, Rh was found to stabilize a clathrate phase of type I, Ba$_8$Rh$_x$Ge$_{46-x-y}\square_y$. The homogeneity range at 800 °C extends to a Rh content of 1.2 atoms/unit cell at a remaining vacancy content of $y = 2$, accompanied by an increase of the lattice parameter to $a = 1.06932(2)$ nm. Investigating the lattice dynamics of this compound using single-crystal X-ray data revealed features similar to that already reported for other Ge-based clathrates.[4] Phase relations in the Ge-rich part of the Ba−Rh−Ge system are characterized by the existence of two novel compounds, Ba$_3$Rh$_4$Ge$_{16}$ and Ba$_5$Rh$_{15}$Ge$_{35.75}$,

for both of which a new, unique crystal structure was established by single-crystal X-ray measurements.

   The DFT-derived enthalpies of formation for Ba$_8$Rh$_x$Ge$_{46-x}$ support the experimental results, namely, that the incorporation of Rh atoms into the clathrate I framework significantly stabilizes the compound. The DOSs reveal gaps or deep minima, which are linked to the large gap of Ba$_8$Ge$_{46}$ about 1 eV below E_F. The Fermi energy gets closest to a deep minimum for $x = 3$, in line with the valence electron-counting rule, which yields $x_{gap} = {}^{16}/_5$ for the critical concentration.

   The limited homogeneity range of Ba$_8$Rh$_x$Ge$_{46-x-y}\square_y$ prevents this compound from exhibiting interesting thermoelectric properties because the sample with the maximum Rh content, Ba$_8$Rh$_{1.2}$Ge$_{42.8}\square_{2.0}$, still has metallic properties and thus the Seebeck coefficient of -20 μV/K at room temperature remains below thermoelectrically interesting values. The electrical resistivities of BaRhGe$_3$ and Ba$_5$Rh$_{15}$Ge$_{35.75}$ increase with increasing temperature, exhibiting metallic behavior, and for Ba$_5$Rh$_{15}$Ge$_{35.75}$, revealing a 6 times higher residual resistivity ρ_0 (320 $\mu\Omega$ cm), a tendency for saturation above 300 K is observed. Ba$_3$Rh$_4$Ge$_{16}$ shows a superconducting transition at a critical temperature of $T_C = 6.5$ K and the upper critical field is completely suppressed at 1.5 T, close to the predicted value of 1.14 T from the WHH model. The heat capacity data confirmed bulk superconductivity and BCS-like behavior.

■ ASSOCIATED CONTENT

ⓢ Supporting Information
X-ray crystallographic data in CIF format and additional figures and tables. This material is available free of charge via the Internet at http://pubs.acs.org.

■ AUTHOR INFORMATION

Corresponding Author
*E-mail: peter.franz.rogl@univie.ac.at. Tel: +43-1-4277-52456. Fax: +43-1-4277-95245.

Notes
The authors declare no competing financial interest.

■ REFERENCES

(1) Slack, G. A. In *CRC Handbook of Thermoelectrics*; Rowe, D. M., Ed.; CRC Press: Boca Raton, FL, 1995; Vol. *407*.
(2) Nolas, G. S.; Cohn, J. L.; Slack, G. A.; Schujman, B. *Appl. Phys. Lett.* **1998**, *73* (2), 178.
(3) Nolas, G. S.; Slack, G. A.; Schujman, S. B. In *Semiconductors and Semimetals*; Tritt, T. M., Ed.; Academic Press: New York, 2001; Vol. 69, pp 255−300.
(4) Christensen, M.; Johnsen, S.; Iversen, B. B. *Dalton Trans.* **2010**, *39*, 978−992.
(5) Kleinke, H. *Chem. Mater.* **2010**, *22*, 604−611.
(6) Grytsiv, A.; Melnychenko-Koblyuk, N.; Nasir, N.; Rogl, P.; Saccone, A.; Schmid, H. *Int. J. Mater. Res.* **2008**, *100*, 189−202.
(7) Cordier, G.; Woll, P. *J. Less-Common Met.* **1991**, *169*, 291−302.
(8) Czybulka, A.; Kuhl, B.; Schuster, H. U. *Z. Anorg. Allg. Chem.* **1991**, *594*, 23.
(9) Carrillo-Cabrera, W.; Budnyk, S.; Prots, Y.; Grin, Y. *Z. Anorg. Allg. Chem.* **2004**, *630*, 2267−2276.

(10) Roisnel, T.; Rodriguez-Carvajal, J. *Mater. Sci. Forum* **2001**, *118*, 378−381.

(11) Sheldrick, G. M. *Acta Crystallogr.* **1990**, *A46*, 467−473.

(12) Kresse, G.; Furthmueller, J. *Phys. Rev. B: Condens. Matter* **1996**, *54*, 11169. Kresse, G.; Furthmueller, J. *Comput. Mater. Sci.* **1996**, *6*, 15.

(13) Ceperley, D. M.; Alder, A. B. *Phys. Rev. Lett.* **1980**, *45*, 566.

(14) Bloechl, P. E. *Phys. Rev. B* **1994**, *50*, 17953.

(15) Kresse, G.; Joubert, D. *Phys. Rev. B* **1999**, *59*, 1758.

(16) Monkhorst, H. J.; Pack, J. D. *Phys. Rev. B* **1976**, *13*, 5188.

(17) Okamoto, H. *J. Phase Equilib. Diffus.* **2009**, *30* (1), 114.

(18) Carrillo-Cabrera, W.; Borrmann, H.; Paschen, S.; Baenitz, M.; Steglich, F.; Grin, Y. *J. Solid State Chem.* **2005**, *178* (3), 715−728.

(19) Pani, M.; Palenzona, A. *J. Alloys Compd.* **2008**, *462*, L9−L11.

(20) Massalski, T. B. *Binary Alloy Phase Diagrams*, 2nd ed.; ASM International: Materials Park, OH, 1990; pp 1989−1991.

(21) Teatum, E.; Gschneidner, K.; Waber, J. *LA-2345*; U.S. Department of Commerce: Washington, DC, 1960.

(22) Nasir, N.; Melnychenko-Koblyuk, N.; Grytsiv, A.; Rogl, P.; Giester, G.; Wosik, J.; Nauer, E. *J. Solid State Chem.* **2010**, *183*, 565−574.

(23) Aydemir, U.; Akselrud, L.; Carillo Cabrera, W.; Candolfi, C.; Oeschler, N.; Baitinger, M.; Steglich, F.; Grin, Y. *J. Am. Chem. Soc.* **2010**, *132* (32), 10984−10985.

(24) Melnychenko-Koblyuk, N.; Grytsiv, A.; Fornasari, L.; Kaldarar, H.; Michor, H.; Rohrbacher, F.; Koza, M.; Royanian, E.; Bauer, E.; Rogl, P.; Rotter, M.; Schmid, H.; Marabelli, F.; Devishvili, A.; Doerr, M.; Giester, G. *J. Phys.: Condens. Matter* **2007**, *19*, 26.

(25) Nguyen, L. T. K.; Aydemir, U.; Baitinger, M.; Bauer, E.; Borrmann, H.; Burkhardt, U.; Custers, J.; Haghighirad, A.; Höfler, R.; Luther, K. D.; Ritter, F.; Assmus, W.; Grin, Y.; Paschen, S. *Dalton Trans.* **2010**, *39*, 1071−1077.

(26) Falmbigl, M.; Rogl, G.; Rogl, P.; Kriegisch, M.; Mueller, H.; Bauer, E.; Reinecker, M.; Schranz, W. *J. Appl. Phys.* **2010**, *108*, 043529.

(27) Koch, E.; Fischer, W. *Z. Kristallogr.* **1996**, *211*, 251−253.

(28) Villars, P.; Cenzual, K. *Pearson's Crystal Data: Crystal Structure Database for Inorganic Compounds (on CD-ROM)*, release 2011/12; ASM International: Materials Park, OH, 2011/2012.

(29) Zeiringer, I.; Chen, M. X.; Bednar, I.; Royanian, E.; Bauer, E.; Podloucky, R.; Grytsiv, A.; Rogl, P.; Effenberger, H. *Acta Mater.* **2011**, *59*, 2368.

(30) Yan, X.; Chen, M. X.; Laumann, S.; Bauer, E.; Rogl, P.; Podloucky, R.; Paschen, S. *Phys. Rev. B* **2012**, *85*, 165127.

(31) Falmbigl, M.; Chen, M. X.; Grytsiv, A.; Rogl, P.; Royanian, E.; Michor, H.; Bauer, E.; Podloucky, R.; Giester, G. *Dalton Trans.* **2012**, *41*, 8839−8849.

(32) Blatt, F. J. *Physics of Electronic Conduction in Solids*; McGraw-Hill Series in Materials Science and Engineering; McGraw-Hill: New York, 1968.

(33) Gonzalez, J.; Kessens, R.; Schuster, H. U. *Z. Anorg. Allg. Chem.* **1993**, *619*, 13−16.

(34) Wiesmann, H.; Gurvitch, M.; Lutz, H.; Ghosh, A.; Schwarz, B.; Strongin, M.; Allen, P. B.; Halley, J. H. *Phys. Rev. Lett.* **1977**, *38*, 782.

(35) Werthamer, N. R.; Hefland, E.; Hohenberg, P. C. *Phys. Rev.* **1966**, *147*, 295.

(36) Maki, K. *Phys. Rev.* **1966**, *148*, 362.

(37) Cooper, A. S. *Acta Crystallogr.* **1962**, *15*, 578−582.

(38) Jeitschko, W.; Parthé, E. *Acta Crystallogr.* **1967**, *22*, 417−430.

(39) Parthé, E.; Geelato, L.; Chabot, B.; Penzo, M.; Cenzual, K.; Gladyshevskii, R. *TYPIX Standardized Data and Crystal Chemical Characterization of Inorganic Structure Types*; Springer: Berlin, 1994.

(40) Melnychenko-Koblyuk, N.; Grytsiv, A.; Rogl, P.; Rotter, M.; Bauer, E.; Durand, G.; Kaldarar, H.; Lackner, R.; Michor, H.; Royanian, E.; Koza, M.; Giester, G. *Phys. Rev. B: Condens. Matter Mater. Phys.* **2007**, *76*, 144118.